A Comparison of Alternative Volumetric Dip Computations

Megan Jo Gunther* and Dr. Kurt J. Marfurt

The University of Oklahoma

Introduction

Time and horizon slices through volumetric dip can delineate faults, folds, channel edges, karst collapse, and many other geologic features of interpretation interest. While less commonly used in interpretation presentations than coherence, amplitude, impedance, and even curvature attributes, accurate estimates of volumetric dip are critical to the accurate calculation of all geometric attributes and structure-oriented filtering and is a key component in the emerging seismic geochronology analysis software. Multiple software platforms provide different volumetric dip calculations, with one vendor providing no less than five different algorithms. While not exhaustive, in this case study we apply six of the more common volumetric dip computations to estimate volumetric dip using an offshore New Zealand 3D seismic survey.

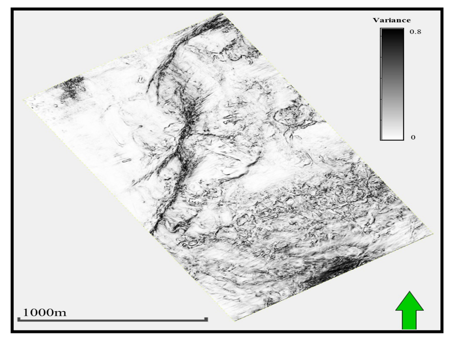

Figure 1: Variance calculated from seismic amplitude.

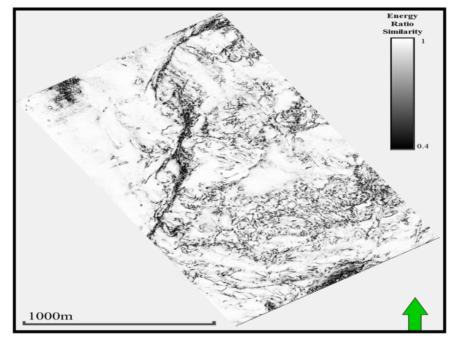

Figure 2: Energy Ratio Similarity calculated using dip magnitude.

Challenges Faced

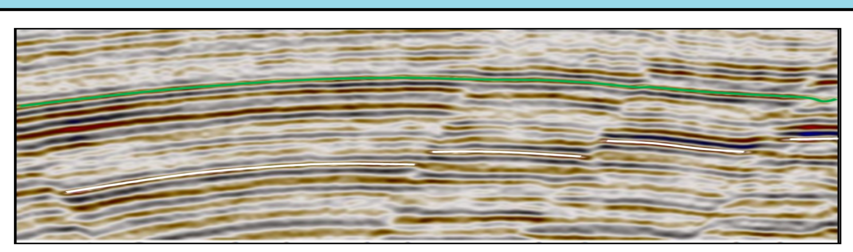

Figure 4: Example of current dip challenges. The green horizon shows incorrect picks due to aliasing while the white horizon shows the correct horizon pick across the fault (Aarre 2010).

- Correlated noise and uncorrelated noise
- Limited temporal and/or lateral resolution
- Instantaneous dip calculations

Main Architectural Elements

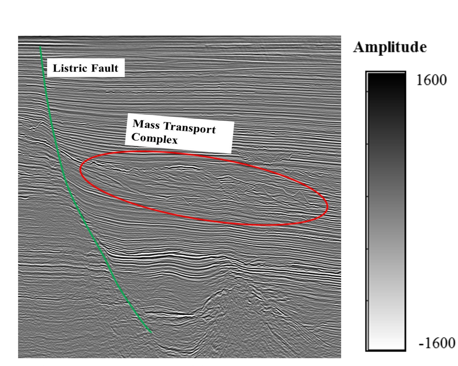

Figure 5: Inline through amplitude showing main architectural elements.

Method 1: Semblance Scan

The semblance scan is calculated over overlapping windows known as the Kuwahara window (Kuwahara et al., 1976). The window with the highest semblance best represents the signal (Marfurt, 2006). The semblance (σ) is shown by Equation 1 and Figure 6.

$$\sigma(t,p,q) \equiv \frac{\left[\frac{1}{J}\sum_{j=1}^{J} u_j(t-px_j-qy_j)\right]^2}{\frac{1}{J}\sum_{j=1}^{J}\left\{\left[u_j(t-px_i-qy_j\right]^2\right\}} \qquad (1)$$

$t = time$

$p, q = apparent\ dip$

$x_j, y_j = x\ and\ y\ directions$

$J = number\ of\ traces$

$u_j = trace$

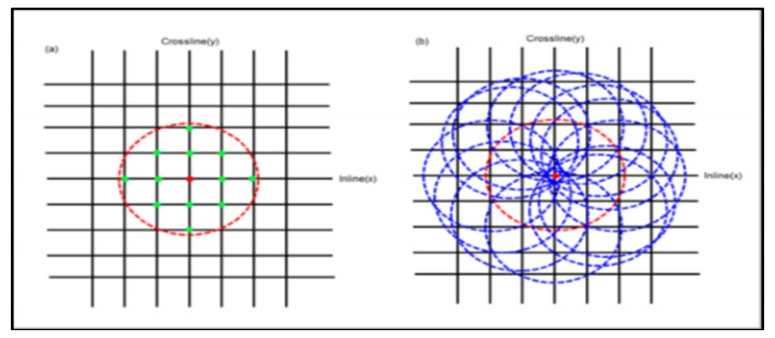

Figure 6: Cartoon describing the Kuwahara filter. The left figure demonstrates a 13 trace circular analysis window centered about the red dot. Each green dot represents a trace which then has its own circular analysis window containing the red dot trace shown on the right image (Marfurt, 2006).

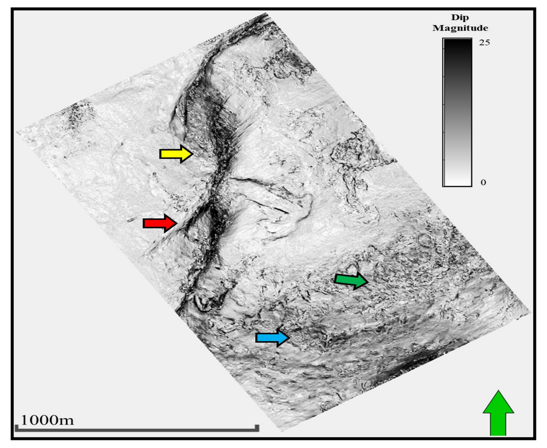

Figure 7: Time slice at t=1437ms through dip magnitude computed using the Kuwahara semblance search. yellow arrow shows the N-S trending listric fault, red arrow shows smaller fault branching off the large faults, the blue arrow shows "salt and pepper" noisy features, and the green arrow shows the mass transport deposition.

Method 2: Event Dip

The event dip calculates the derivatives of the seismic amplitude in the x, y, and z directions, forming a local 3 component vectors.

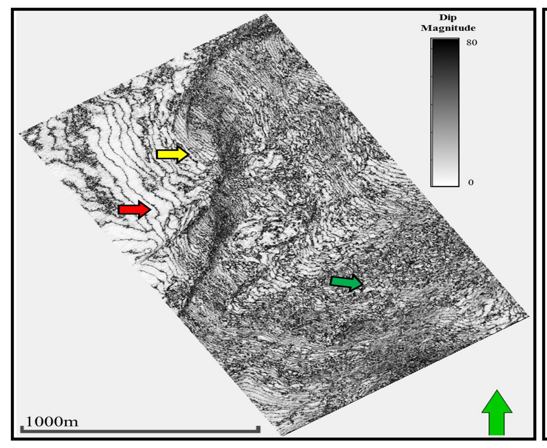

Figure 8: Time slice t=1437ms through the event dip estimation method. The green circle is indicating a noisy area within the data, red arrow shows the contour features associated with the phase changes of the seismic wavelet, and the yellow arrow shows the north-south trending fault.

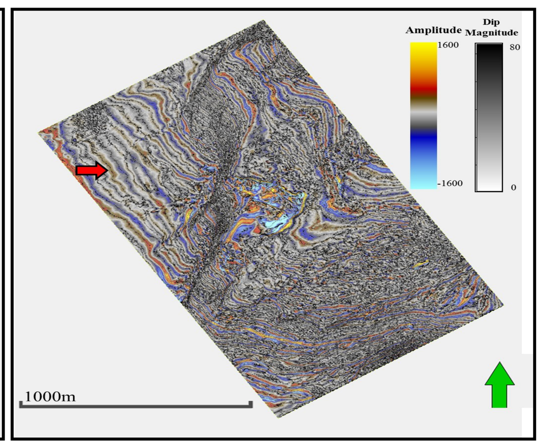

Figure 9: Time slices at t=1437ms of co-render event dip and seismic amplitude. The red arrow demonstrates areas where an artifact occurs where there is a peak event of the seismic wavelet.

Method 3: Gradient Structure Tensor (GST)

The GST is calculated by cross correlating the three derivatives with each other forming a 3x3 GST. The elements of the tensor are then smoothed individually by a low-pass filter. The eigenvector with the largest eigenvalue of the GST matrix is the normal to the plane that best fits the data variability.

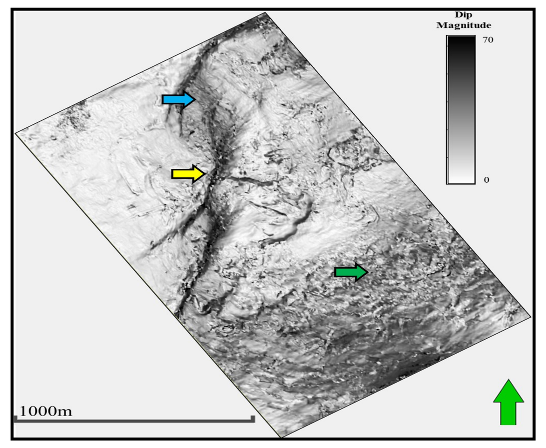

Figure 10: Time slice at t=1437ms through the GST algorithm. The yellow arrow points to a North-South trending listric fault as seen from a vertical slice. The blue arrow shows smearing of the fault. Lastly, green arrow is showing a mass transport deposit.

Method 4: Globally Consistent Dip Estimation

This method is calculated using a global optimization process that calculates the inline and crossline dip components and highlights areas with an unstable solution. The iteration process of GCDE is shown in Chart 1. Four constraints with user defined iterations are imposed onto the algorithm which are reciprocity, causality, consistency, and continuity.

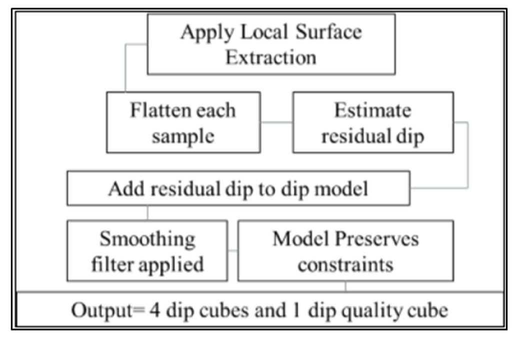

Chart 1: GCDE algorithm workflow with user defined iterations.

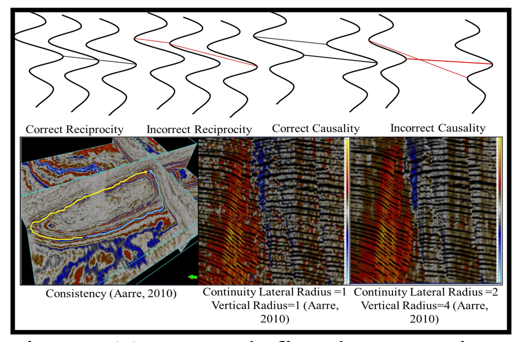

Figure 11: User defined constraints imposed onto the algorithm.

Method 4: Globally Consistent Dip Estimation

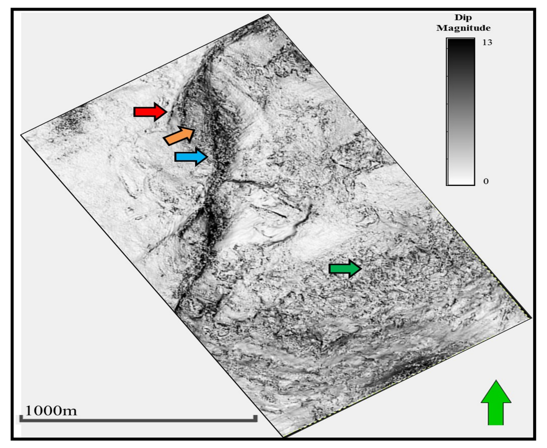

Figure 12: Time slice at t=1437ms through dip magnitude using globally consistent dip estimation method. The blue arrow represents the N-S trending listric faults, red arrow shows smaller faults branching off the large listric faults, green arrow indicates a mass transport complex, orange arrow shows minimal smoothing between the two faults.

Method 5: Dip Steering

This method consists of three dip steering cubes (raw, detailed, and background) and is calculated using either the BG Fast Algorithm or the Fast Fourier Transform (FFT). The concept of dip steering is that attributes are guided along a surface of constant phase (Figure 13) and are calculated from the seismic amplitude data in inline and cross line directions of the extrema (Figure 14).

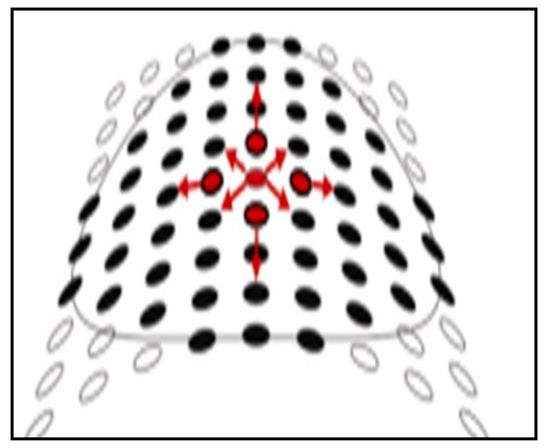

Figure 13: Dip is calculated along a surface of constant phase (dGB Earth Sciences, 2016).

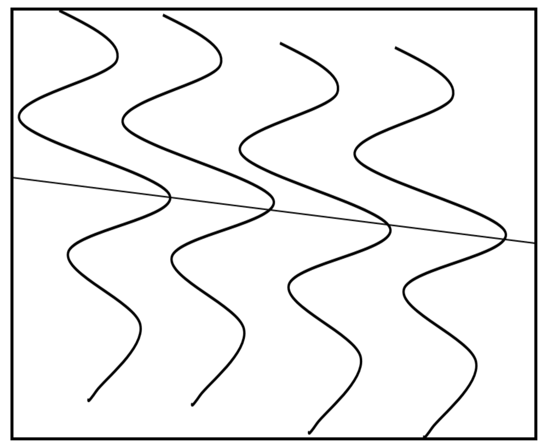

Figure 14: Apparent dips are calculated from both inline and cross line directions from the extrema. All the max and mins are determined by the central trace and its two neighboring traces.

Figures 15-18 show the output of the dip steering method for both the detailed and background steering cube using the Fast Fourier Transform (FFT) and the BG Fast Algorithm.

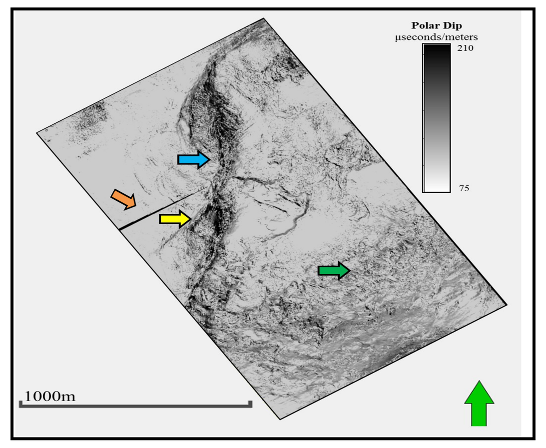

Figure 15: Time slice at t=1437ms through polar dip with units of µseconds/meters. Detailed steering cube calculated using the BG Fast algorithm. The blue arrow shows the N-S trending listric fault, yellow arrow shows finer faults, orange arrow shows some introduced artifact, and the green arrow shows the mass transport complex.

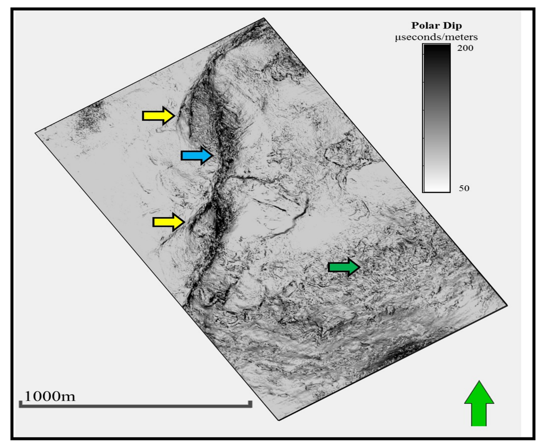

Figure 16: Time slice at t=1437ms through polar dip with units of µseconds/meters. Detailed steering cube calculated using the FFT algorithm. The blue arrow shows the N-S trending listric fault, yellow arrows shows finer faults, and the green arrow shows the mass transport complex.

Method 5: Dip Steering

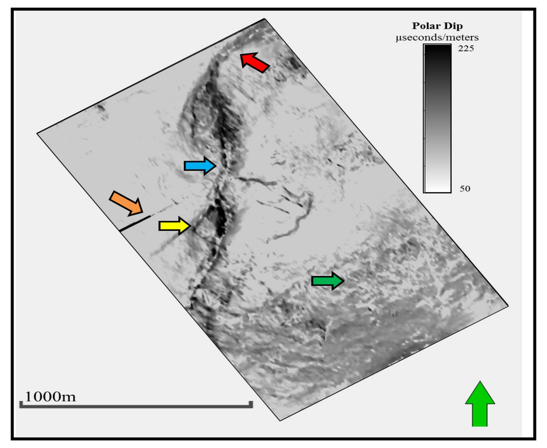

Figure 17: Time slice at t=1437ms through polar dip with units of µseconds/meters. Background steering cube calculated using the BG Fast Algorithm algorithm. The blue arrow shows the N-S trending listric fault, yellow arrow shows smaller scaled faults, green arrow shows the mass transport complex, orange arrow shows some introduced artifact, and the red arrow shows smoothing of the fault.

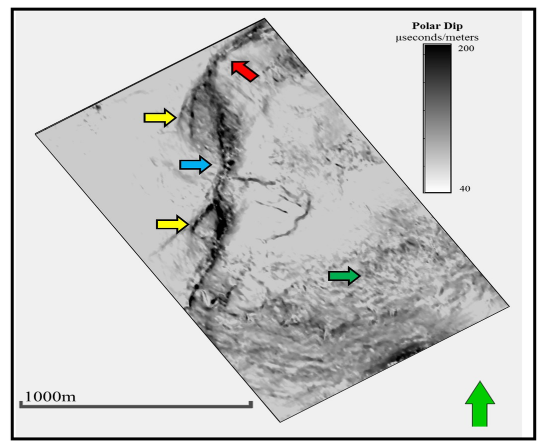

Figure 18: Time slice at t=1437ms through polar dip with units of µseconds/meters. Background steering cube calculated using the FFT algorithm. The blue arrow shows the N-S trending listric fault, yellow arrows show finer fault features, green arrow shows the mass transport complex, and the red arrow shows smoothing.

Method 6: Plane Wave Destructor (PWD)

Fomel (2002) created this method as an initial model for migration. This method builds a three–dimensional filter/operator (destructor) that runs along the seismic volume calculating the dip. Figure 19 shows the output using the PWD.

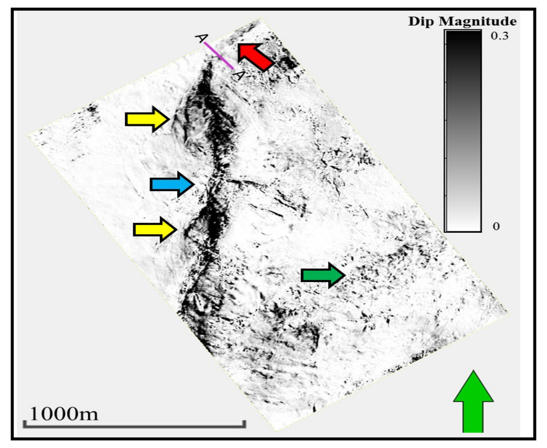

Figure 19: Dip magnitude using the PWD method. Larger scaled features such as the N-S trending listric fault are shown by the blue arrow, red arrow shows smoothing of the fault, green arrow shows the less visible mass transport complex, and the yellow arrows show the smaller faults. A to A' is an arbitrary line.

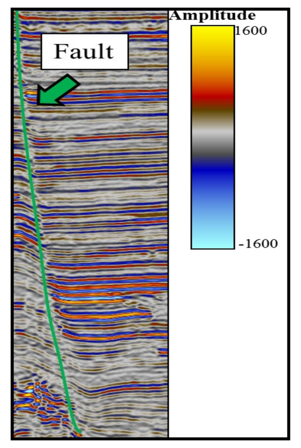

Figure 20: A-A' arbitrary line showing fault not well shown by the red arrow in Figure 19 using PWD.

Conclusions

A comparison of the different algorithmic methods used to estimate volumetric dip Chart 3.

Algorithm	Speed	Artifact Resistant	Noise Resistant	Large Features	Fine Scale Features	Software friendliness
Semblance Scan	Good	Excellent	Good	Excellent	Good	Excellent
Event Dip	Excellent	Worse than Average	Worse than Average	Poor	Worse than Average	Excellent
GST	Excellent	Excellent	Good	Excellent	Good	Excellent
GCDE	Excellent	Excellent	Good	Excellent	Excellent	Excellent
Dip Steering (BG Fast Algorithm)	Worse than Average	Poor	Worse than Average	Excellent	Poor	Poor
Dip Steering (FFT)	Worse than Average	Excellent	Good	Excellent	Good	Poor
Plane Wave Destructor	Poor	Excellent	Excellent	Good	Worse than Average	Worse than Average

Excellent Good Poor Worse than Average

Chart 3: Customer review chart used for method comparison.

Acknowledgments

Thank you to the industry sponsors of the Attribute-Assisted Processing and Interpretation (AASPI) consortium for the support throughout this study and Fangyu Li for his help and guidance. A special thanks to Schlumberger, dGB, Madagascar, and AASPI for the use of their software in research and education.

References

Aarre, V. (2010, January). Globally consistent dip estimation. In *2010 SEG Annual Meeting*. Society of Exploration Geophysicists.

Astratti, D., Aarre, V., Vejbæk, O. V., & White, G. (2015). Mapping and time-lapse analysis of South Arne Chalk fault network using new developments in seismic dip computation. *Geological Society, London, Special Publications*,*406*(1), 331-358.

Brouwer, F. (2007). Creating a good Steering Cube. *Available on*.

dGB Earth Sciences, 2016, 3 Dip-Steering, http://www.opendtect.org/600/doc/dgb_userdoc/Default.htm#dip-steering.htm%3FTocPath%3D3%20Dip-Steering%7C_____0

Qayyum, F., Groot, P. Introduction to the Steering Cube. *Available on.*

Randen, T., Monsen, E., Signer, C., Abrahamsen, A., Hansen, J. O., Sæter, T., ... & Sønneland, L. (2000, August). Three-dimensional texture attributes for seismic data analysis. In *70th Annual International Meeting, Society of Exploration Geophysics Expanded Abstracts, Calgary, Canada* (pp. 668-671).

Klokov, A., & Fomel, S. (2012). Separation and imaging of seismic diffractions using migrated dip-angle gathers. *Geophysics*, *77*(6), S131-S143.